

## Slip vector analysis with high resolution t-LiDAR scanning

Thomas Wiatr<sup>a,\*</sup>, Klaus Reicherter<sup>a</sup>, Ioannis Papanikolaou<sup>b</sup>, Tomás Fernández-Steeger<sup>c</sup>, Jack Mason<sup>a</sup>

<sup>a</sup> RWTH Aachen University, Institute of Neotectonics and Natural Hazards, Lochnerstr. 4-20, 52064 Aachen, Germany

<sup>b</sup> Laboratory of Mineralogy & Geology, Department of Sciences, Agricultural University of Athens, 75 Iera Odos Str., 11855 Athens, Greece

<sup>c</sup> RWTH Aachen University, Department of Engineering Geology and Hydrogeology, Lochnerstr. 4-20, 52064 Aachen, Germany

### ARTICLE INFO

#### Article history:

Received 10 January 2013

Received in revised form 5 June 2013

Accepted 20 July 2013

Available online 31 July 2013

#### Keywords:

t-LiDAR

Slip vector analysis

Active bedrock normal fault scarp

Kinematic indicators

Spili Fault

Crete

### ABSTRACT

A palaeostress analysis of an active bedrock normal fault scarp based on kinematic indicators is reconstructed using terrestrial laser scanning (TLS). For this purpose, three key elements are necessary for a defined region: (i) the orientation of the fault plane, (ii) the orientation of the slickenside lineation or other kinematic indicators, and (iii) the sense of motion of the hanging wall. The paper specifies a workflow in order to obtain stress data from point cloud data using terrestrial laser scanning (TLS) in an active tectonic environment.

The entire analysis was performed on a continuous limestone bedrock normal fault scarp on the island of Crete, Greece, at four different locations along the WNW–ESE striking Spili Fault. At each location we collected data with the terrestrial light detection and ranging system (t-LiDAR). We then validated the calculated three-dimensional stress results at three of the locations by comparison with conventional methods using data obtained manually with a compass clinometer. Numerous kinematic indicators for normal faulting were discovered on the fault plane surface using t-LiDAR data. When comparing all reconstructed stress data obtained from t-LiDAR to that obtained through manual compass measurements, the degree of fault plane orientation divergence is  $\pm 005/03$  for dip direction and dip. The degree of slickenside lineation divergence is  $\pm 003/03$  for dip direction and dip. Therefore, the percentage threshold error of the individual vector angle at each investigation site is lower than 3% for the dip direction and dip for planes, and lower than 6% for the strike. The maximum mean variation of the complete calculated stress tensors is  $\pm 005/03$ .

© 2013 Elsevier B.V. All rights reserved.

### 1. Introduction

Palaeostress analysis is used to reconstruct stress field variations for a defined region throughout different geological periods. In particular, the analysis of neotectonic fault segments and their stress field orientations is essential for the investigation of present-day geodynamics, fault kinematics, recent seismic events, potential reactivations of fault segments, and for the evaluation of the fault activity. Furthermore, natural fault scarps and exhumed fault plane segments are indicators of shallow earthquake activity with earthquakes that cut the entire seismogenic layer, involving magnitudes greater than  $M_s > 6$  (Stewart and Hancock, 1990).

Study of normal faults has shown that slip-directions vary with throw and distance, converging towards the fault hanging walls (Roberts, 1996; Maniatis and Hampel, 2008; Michetti et al., 2000). Indeed, the hanging wall of normal faults is stretched along strike because hanging wall subsidence is greater than footwall uplift and fault throw is greatest at fault centres whereas it decreases to zero at the fault tips (Ma and Kusznir, 1995; Roberts, 1996). Fault lengths should therefore be reflected in the length-scale of the converging

patterns of fault slip; as a result they have also been used as an indicator for defining fault lengths (Papanikolaou and Roberts, 2007; Roberts and Michetti, 2004).

For palaeostress reconstruction, we need to obtain some key elements in order to define the fault character, its geometry and the sense and direction of motion. Fault segments have to be characterised and described for deciphering the fault evolution in a specific area. Therefore, the fault plane orientation, the orientation of slickenside lineation and the shear sense of motion, i.e. the movement of the hanging wall, have to be determined. The varying scales of structural heterogeneity, discontinuous geometry along the exhumed footwall slip plane, and the complexity of the surface features like subslip-plane breccia sheets, brecciated colluvium or frictional water-wear striations on the rupture plane, make it difficult to recognise palaeovection indicators on natural fault scarps above the level of exhumation (Roberts, 1996; Stewart and Hancock, 1991). Nevertheless, several authors have published, described and classified tectonic normal fault structures, slickensides and other important kinematic indicators, at different scales, in order to identify the shear sense on active normal faults (Doblas, 1998; Doblas et al., 1997; Hancock and Barka, 1987). For our study we used an artificially exhumed slip plane, a fresh fault scarp above the level of exhumation, a degraded fault scarp and an unbrecciated Quaternary colluvium for metre scale descriptions to determine the fault kinematics (Hancock and Barka, 1987). In

\* Corresponding author. Tel.: +49 2412098430.

E-mail address: [t.wiatr@nug.rwth-aachen.de](mailto:t.wiatr@nug.rwth-aachen.de) (T. Wiatr).

addition, at the tens of centimetre scale, eleven major groups of slickenside kinematic criteria on the exhumed fault plane were used (see Doblas, 1998).

Some recent studies on active fault planes using terrestrial laser scanning (TLS) have indicated that the investigative technique is applicable for morphotectonic analysis (Candela et al., 2009; Jones et al., 2009; Sagy et al., 2007). Using TLS allows data to be collected in dangerous, steep and inaccessible outcrops (Nguyen et al., 2011). Moreover, virtual geometric measurements (Kokkalas et al., 2007) and statistic calculations (Candela et al., 2009; Sagy et al., 2007) of natural fault scarps can also be obtained.

This paper presents a remote sensing solution for slip vector reconstruction in an active tectonic regime using a t-LiDAR system. The test site was on the Spili Fault, which is an active normal fault in limestone bedrock located on the island of Crete in the Aegean region. All measurements of the fault plane, slickenside lineations and slickenside kinematics were performed through analysis of terrestrial remote sensing data and accompanied also with a conventional compass and clinometer so that a comparison can be made. Extension direction analysis was carried out for both data sets and the results were compared.

### 1.1. Location

The island of Crete (Greece) is located north of the Hellenic trench and south of the volcanic arc in the external Hellenides and is associated with the Oligocene/Miocene high pressure/low temperature belt (Fassoulas et al., 1994). Crete is characterised by a complex geological and tectonic structure that results from: i) the successive thrusting of the alpine geotectonic units on top of each other (Bonneau, 1984), ii) the activity of major detachment faults (Fassoulas et al., 1994; Papanikolaou and Vassilakis, 2010; Zachariasse et al., 2011), and iii) the intense neotectonic and active faulting (Caputo et al., 2010; Monaco and Tortorici, 2004; Peterek and Schwarze, 2004).

Crete has undergone uplift of around 2.5 km since the Early Tortonian (Miocene) in several different phases (Meulenkamp et al., 1994). The most recent phase of uplift as evidenced by the uplifted Messinian deposits (Krijgsman, 1996) began at around 6 Ma and continue up to the present day. This is evidenced by the sudden uplift of max. 9 m in AD 365 caused by an earthquake on the plate boundary with an estimated magnitude of  $M > 8$  (Fassoulas, 1999; Meulenkamp et al., 1988; Scheffers and Scheffers, 2007; Stiros, 2001).

Crete has a complex pattern of fault zones due to the island's tectonic evolution. There are two major groups of active normal fault strike directions located on the island (Fig. 1a); many of the associated fault scarps are very impressive and late Quaternary in age. The first group is the WNW–ESE trending faults with north and south dipping fault plane segments, which are principally located in the central southern Crete. Caputo et al. (2010) define four active major normal fault segments within this group including the Sfakia Fault, the Asomatos Fault, the Agia Galini Fault and the Spili Fault; these four fault segments have a cumulative length of around 55 km. The second group is the NNE–SSW trending normal fault segments. These faults are distributed throughout the entire island. The major faults and fault zones of this group are the Phalasarua Fault, Gramvousa Fault, Rodopos Fault Zone, Asterussia Fault, Eastern Psiloritis Fault Zone, Giouchtas Fault, Kastelli Fault, Ierapetra Fault Zone and Sitia Fault Zone (from west to east).

### 1.2. The Spili Fault

The Spili Fault is located in the southern part central Crete. This fault belongs to the group of WNW–ESE trending normal faults dipping to the south (see Fig. 1b). The fault extends over the southern slope of the Kedros ridge (around 1600 m a.s.l.) and has a total length of 20 to 25 km (Monaco and Tortorici, 2004; Mouslopoulou et al., 2011). The

elevation of the Spili Fault varies from west to east. The altitude in the western segment ranges from around 400 m to 900 m a.s.l., the middle segment from around 800 to 600 m a.s.l., and the eastern segment slopes down to around 200 m a.s.l. (see Fig. 1c). The footwall primarily consists of Mesozoic carbonates of the Pindos limestone unit and is partly comprised of the Tripoli limestone unit. The hanging wall comprises formations of alluvial and colluvial deposits.

The Spili Fault has a clear exposed postglacial fault scarp with a maximum height of 8–10 m. The fault scarp is predominantly a free face; however, in localities it is also partly exposed by selective erosion and anthropogenic intervention. All main characteristics across the scarp can be observed such as the artificially exhumed slip planes, the fresh fault scarp above level of exhumations, the free face, the degraded fault scarp and the unbrecciated colluvials. On the fault plane there are various slickenside kinematic indicators such as lineations, plucking markings, tension fractures, hybrid fractures and asymmetric cavities with congruous steps (Fig. 2). Towards the tips of the fault the lineations are continuously inclined pointing towards the hanging wall centre of the fault. Our investigations were carried out at four locations along the exposed fault. At location 1, which is also the sample area from Mouslopoulou et al. (2011) (Fig. 2.1a–d), there is an impressive fault plane containing tension gashes, slickenside lineations, pluck holes and spall marks (Fig. 2.1b). Furthermore, two types of fault gouge are present (Fig. 2.1c), and the eastern part of the fault segment separates into four sub-slip fault planes (Fig. 2.1d). At location 2, the fault plane has been artificially excavated revealing a colluvial wedge. Above the excavated fault plane, the surface is weathered and is increasingly vegetated (see Fig. 2.2e). Locations 3 and 4 are situated near a canyon close to the village Kria Vrisi. The exhumed fault scarp has tension gashes and karstic features (Fig. 2.3f, 4). Some areas on the fault plane contain no kinematic indicators as erosion has completely erased them. However, calcite fibres are present which are located up to 40 cm above the underlying colluvium. Moreover, lineations, breccia sheets, polished fault plane surfaces and corrugated slip planes can also be observed.

V-shaped canyons and wind gaps are also present on the footwall mountain ridge in the north. Moreover, earthquake archaeological effects are described at the archaeological site of Phaistos, located around 20 km south-east of the Spili Fault; the site dates back to Minoan era between 4000 and 1350 B.P. (Monaco and Tortorici, 2004). These factors all indicate that the Spili Fault is active.

## 2. Data acquisition

Our investigation on the Spili Fault was carried out at four locations along the exposed fault escarpment (Fig. 1b). These areas comprise the middle segment of the fault and cover a distance of 10 km. The individual locations have exposed fault planes up to several metres in height. The locations also contain a variety of useful kinematic features (subslip-plane breccia sheet, corrugated slip plane, brecciated colluvium, polished surfaces, degraded fault scarps and slickensides), which can be used to calculate palaeostress. The variation in scarp height can be explained by erosion, variable deposition on the drainage network, anthropogenic intervention and also by the along strike variability of slip along strike of the fault. The kinematic indicators used for palaeostress analysis come in diverse units of scale. The scale of indicators ranges from microscopic, to tens of millimetres, all the way up to metres (Doblas et al., 1997; Hancock and Barka, 1987). Kinematic indicators of microscopic scale could not be measured in the field. This is due to the resolution constraints of the t-LiDAR instrument. However, all other indicators on the fault plane were measured such as corrugations, fractures and calcite fibres.

To reconstruct the palaeostress regime, the orientation of both the fault plane and kinematic indicators must be analysed. For that reason, four measurements on the exhumed fault plane need to be carried out in the field: (i) the dip direction of the fault plane must be measured to determine the spatial orientation; (ii) the dip angle of the fault plane;

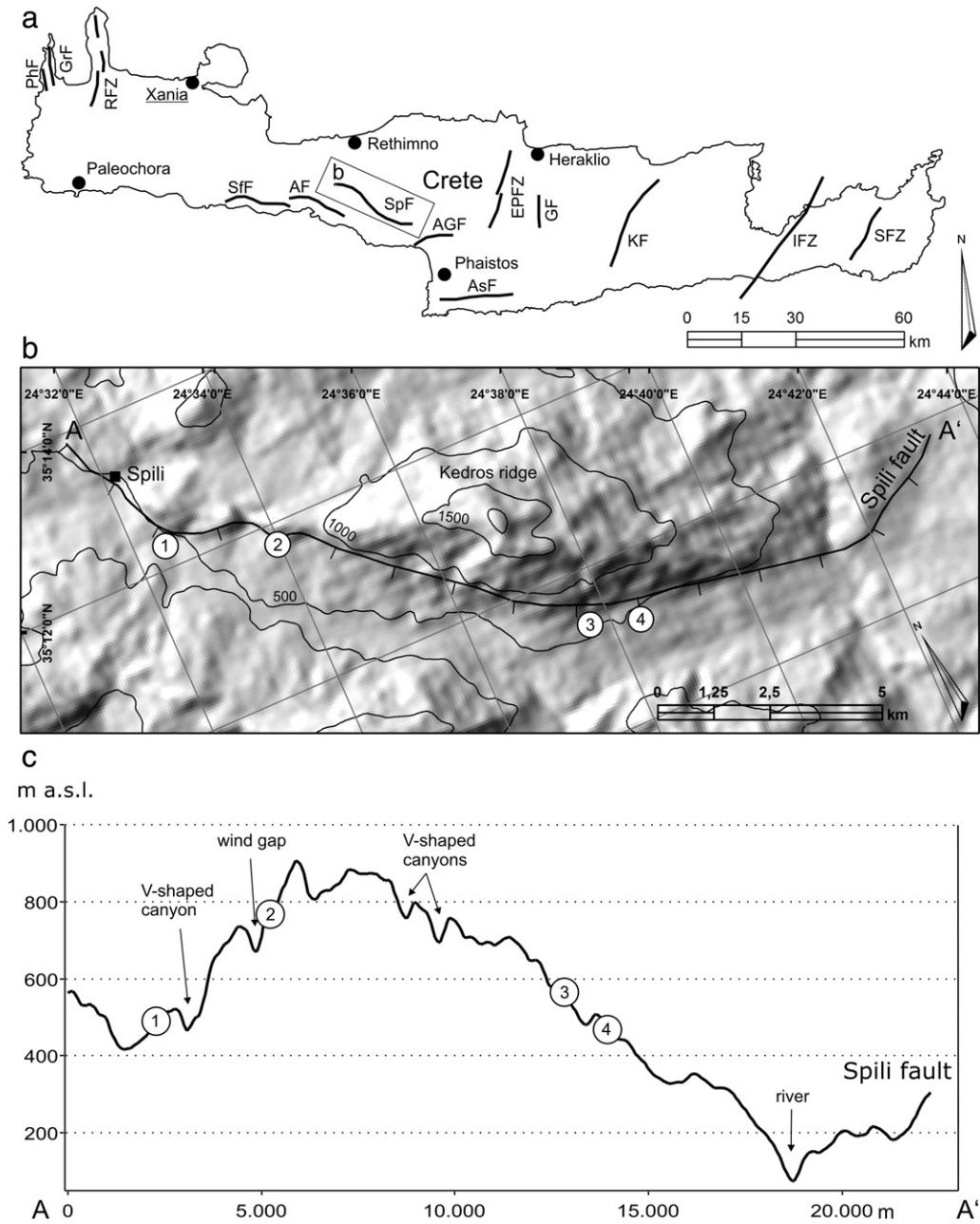


**Fig. 1.** (a) Simplified tectonic map of Crete including the two major fault zone orientations which comprise WNW–ESE and NNE–SSW trending faults (based on Caputo et al., 2010). SfF: Sfakia Faults; AF: Asomatos Faults; SpF: Spili Fault; AGF: Agia Galini Fault; PhF: Phalasarina Fault; GrF: Gramvousa Fault; RFZ: Rodopos Fault Zone; AsF: Asterussia Fault; EPFZ: Eastern Psiloritis Fault Zone; GF: Giouchtas Fault; KF: Kastelli Fault; IFZ: Ierapetra Fault Zone; SFZ: Sitia Fault Zone. (b) Overview map (SRTM based). The numbers are the locations of the field and LiDAR investigation along the strike of the Spili Fault. (c) Elevation profile along the strike from west to east along the Spili Fault including a wind gap, V-shaped canyons and the river.

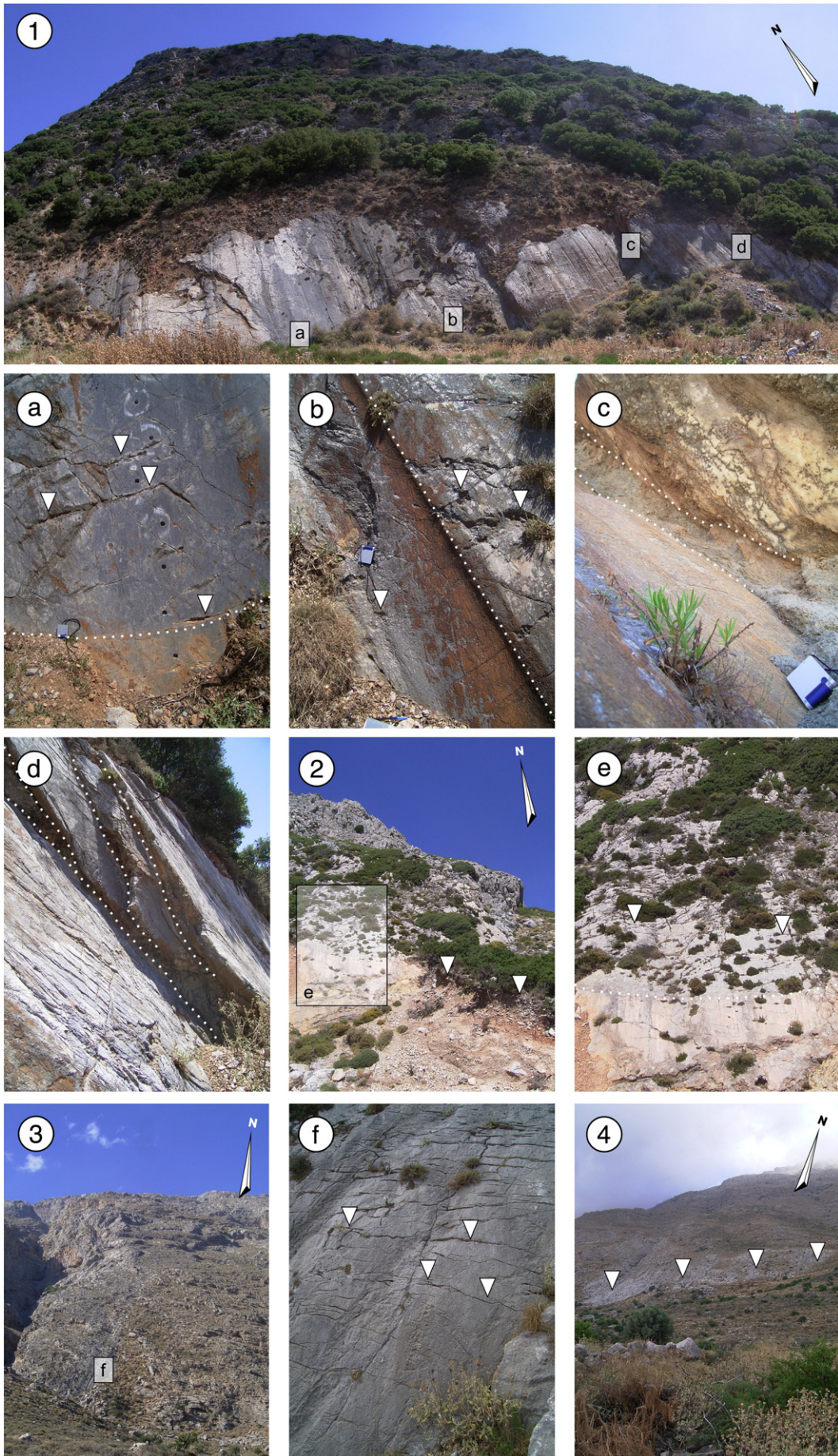
(iii) the dip direction of the slickenside lineation to determine the orientation of movement; and (iv) the dip angle of the slickenside lineation to determine the gradient (Angelier, 1994). The first two angles (dip direction and dip angle) allow the orientation of the fault plane to be described. The second two angles (dip direction and dip of slickensides) allow the slip vector of movement along the fault plane to be calculated. These four measurements were carried out in the field using a conventional compass clinometer and in retrospect using the t-LiDAR data. At locations 1, 2 and 3 (Fig. 1b), both manual field measurements and t-LiDAR scanning were undertaken to allow for a comparison of results. At location 4, however, only t-LiDAR was undertaken. This was due to the inaccessibility of fault plane surface which is located to the east of location 3.

The identification of all kinematic indicators along the investigated fault segment is usually limited. This is due to kinematic indicators not

all being present at one location, they have been altered by external processes, or they are too small for the laser scanner’s spatial resolution to define. In order to gain as much kinematic data as possible, field measurements of the main eleven normal fault scarp slickenside kinematic indicators (Doblas, 1998) were carried out. These included: crescentic markings, steps, fractures, trailed material, asymmetric elevation, deformed elements, asymmetric plan-view fractures, asymmetric cavities, asymmetric folds and mineralogical crystallographic orientations, which were all present on the Spili Fault surface.

2.1. t-LiDAR

The t-LiDAR (terrestrial Light Detection And Ranging) or TLS (terrestrial laser scanning) remote sensing method has been established as a versatile data acquisition tool in photogrammetry, engineering



technologies, atmospheric studies, geoscience and geological engineering in areas which are difficult to access (Brenner, 2005; Nguyen et al., 2011). The technique is a non-contact, non-destructive and non-penetrative active recording system, and the high spatial and temporal resolution makes it an effective method for combining morphological reconstructions and geological settings (Schumann et al., 2011), monitoring, numerical modelling and observations of geological phenomena (Hu et al., 2012).

t-LiDAR generates a coherent laser beam with little divergence by stimulated emission. The electromagnetic waves are reflected by surfaces and the receiver detects portions of the backscattered signal. In our study, we used the laser ranging system ILRIS 3D from Optech Inc., Ontario, Canada.

The advantages of the terrestrial method are the flexible handling, the relatively quick availability of an actual data set with a recording frequency of 2500 points per second, and the very high spatial resolution of the data set (depending on the range between scanner and object). Information about reflected laser beam intensity ranges between 0 (low) and 255 (high) without scale unit and the spatial information is recorded in x–y–z-coordinates. The quality of the reflection data depends on the inclination angle of the laser beam, the range between the object and scanner, the material, the colour, the surface condition and the spatial resolution. The laser wavelength of our system is 1500 nm.

In combination with a digital camera, the point cloud can merge with panchromatic information (RGB); the Optech laser scanner has an integrated 6-megapixel camera. Laser scanning allows 3D surface data acquisition, which is specifically characterised by a digital data record and computerised data analysis. The application of the ILRIS 3D is limited by high precipitation, fog, snow, low target reflectivity, a high cumulative distance of more than 600 m and a shallow incident angle. However, in the frame of this study, these drawbacks are minimised by the close investigation range, i.e. the relatively small distance between the t-LiDAR scanner and the fault plane. Hence, the footprint is small-sized, so that the reflectivity is high and minimum spot steps can be used. In addition, the angle of incidence of the laser beam is perpendicular to the target (close to 90°). For our study the distance between the t-LiDAR and the scarp ranged between 5 m and 100 m, thus offering a maximum resolution of several millimetres (mm) and excellent data quality. Furthermore, the outcrop of the fault plane was scanned multiple times from different vertical and horizontal directions to minimise data shadow effects.

The main aims of the investigation were to utilise t-LiDAR in order to: (i) find quantitative and qualitative solutions for the reconstruction of fault plane surfaces, and (ii) determine the palaeostress regime based on fault slip data of active faults in limestone. In this context, the detailed structural analysis of rock surfaces is fundamental and can be realised using a high resolution digital elevation model (HRDEM).

To ensure data quality and to allow for the reconstruction of palaeostress, we scanned the Spili Fault Zone at four different locations along the fault strike (see Fig. 1b, 2). At locations 1 and 4, the fault surface was scanned with two overlapping scan windows; at locations 2 and 3, one scan window was sufficient. A point to point resolution between 2 mm (at locations 1 and 2) and 28 mm (at the locations 3 and 4) was chosen for the different point clouds. At these sites the raw point cloud data has around 14 million points (see Table 1). At locations 1 and 2, we used t-LiDAR for close range investigations, and at locations 3 and 4 we applied t-LiDAR for long range investigations. During the t-LiDAR field measurements, the scanning direction and roll and pitch angle were measured manually with a compass and inclinometer; the

position of the t-LiDAR was also documented using GPS. These data are essential for processing and palaeostress reconstruction.

### 3. Data processing

t-LiDAR raw data processing was carried out using the PolyWorks (InnovMetric, 2010) software package. The first step for every scan location was to import the individual single scan windows in the alignment tool of PolyWorks. Each point cloud of one scan project includes their associated relative coordinate system. This allows scan projects with more than one scan sequence to be transformed into one system. The alignment of following scans starts manually by identifying points in elements with a distinctive geometry. After that, an automated point-to-surface Iterative Closest Point (IPC) algorithm was applied in order to minimise the co-registration error. This lowers the maximum difference to 0.05 mm and reduces the deviation tolerance to 0.5 mm. Different scan sequences overlap by 20% to ensure good matching (Nguyen et al., 2011). Manual removal of the vegetation was performed by selecting and removing the affected points above ground level. Also, uninteresting areas and areas containing non-geological features were selected and cleared.

To georeference the point clouds, the first imported scan window and the GPS data were used to define the scanner position. To get the right orientation of the scan sequences, the recorded scanner view direction was used for the northing and the pitch and roll angle for horizontal and vertical correction.

Subsequently, two sets of data were generated for every scanned location; for both sets the georeferenced and orientated scan data was used. One data set was created for orientation analysis of the fault plane and slip vector in the software packages PolyWorks and SplitFx. The other data set was used for spatial morphological analysis in a geographical information system (GIS); we used ArcMap version 10 from ESRI.

#### 3.1. Spatial morphological analyses in GIS

After data validation, georeferencing, spatial orientation and data cleaning, the point cloud for the GIS analysis was rotated to a horizontal plane. However, the inclination angle of the fault surface remained and the relative morphological changes on the fault plane are preserved. This point cloud was then imported into ArcMap and has been processed like a typical digital elevation model (DEM). In GIS, the imported point cloud was converted into a triangulated irregular network (TIN) and transformed into a raster format with the corresponding resolution of point to point spacing (see Fig. 3a–b). This occurred because with the grid format it is then possible to quantify morphological features. In this study we used GIS to extract the orientation of kinematic indicators in areas of interest and to identify homogenous areas by undertaking morphological analyses (e.g. slope angle, aspect, curvature, contour lines and hillshades). For instance, we used hillshade to get a morphological overview of the whole scan sequence. The slope angle analysis is useful for edging detection on the plane in a spatial environment (Fig. 3d; red colour specify slopes between 70° and 90°), and the aspect, as seen in Fig. 3g, shows revealing data about the down-slope (red colour) or up-slope (turquoise colour) direction into the fault plane surface of the edges. All this information is needed and helpful for kinematic criteria decisions, such as the sense of the motion such or geometric characterisation. The contour lines are used to determine the height of the identified phenomena (see Fig. 3f). Monochromatic wavelength information, or the detected backscattered intensity (without scale unit),

**Fig. 2.** Photo plate of the different investigation locations along the strike direction of the Spili Fault; location numbers 1–4 (see Fig. 1). At location 1 there is an impressive fault plane with tension gashes; (a) the sample area from Mouslopoulou et al. (2011); (b) slickenside lineation, pluck holes and spall marks on the fault plane; (c) two types of fault gauges are exposed; (d) the plane graduates into four sub-slip fault planes in the eastern part of the outcrop. Location 2 is anthropogenically influenced and a colluvial wedge can be observed; (e) above the excavation the effects of weathering and vegetation density increases. Locations 3 and 4 are situated near a canyon close to the village Kria Vrissi; (f) at location 3 the exhumed fault has tension gashes and karstic features.

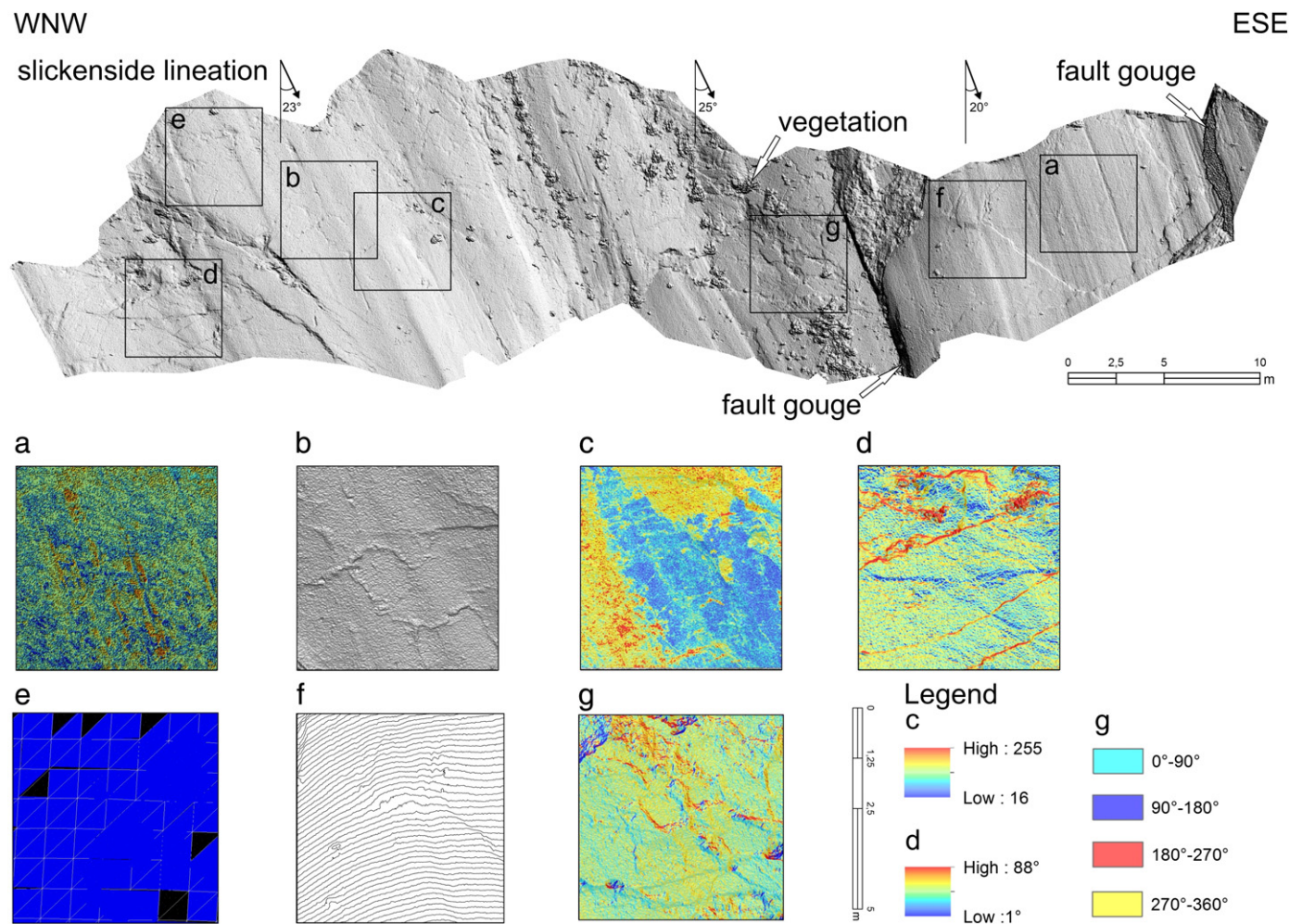


**Fig. 3.** A fault segment example from location 1 showing an overview of the fault plane and the different analytical tools in the detail boxes (a–g) used for morphological analyses; the lineation and kinematic indicator orientation were determined in a three-dimensional spatial way using different software packages. (a) From the point cloud a TIN was generated; (b) Raster data set produced in GIS; (c) Backscattered signal of x, y, and z attributes from the raster data. In GIS the morphological analysis of: (d) slope, (f) contour lines and (g) aspect were realised. (e) Georeferenced and orientated meshed point clouds were used for the plane orientation and patches were transcribed using SplitFx software (the picture is not in scale).

reflects the surface properties in the near infrared that are not spotted by human eye. Hence, we used the backscattered intensity to identify a number of significant tectonic fault conditions such as breccias, fractures, and degraded and polished parts of the fault surface. Fig. 3c shows these fault conditions where the low values (blue) show the polished part of the fault surface and high values (red) indicate the breccia sheet. Therefore, morphological analyses can be useful for fault plane surface topography definition to highlight the kinematics complexity of the fault, and also to determine adequate sampling localities, e.g. for cosmogenic dating.

To determine the orientation of kinematic indicators we carried out a detailed study of the areas of interest. Different forms of kinematic indicators were extracted and topographic profiles across the scarp were produced to determine their geometric characteristics.

### 3.2. Fault plane orientation, kinematic criteria and slip vector analysis

For each study location, a subsampled point cloud with uniformed 0.10 m point spacing was exported from the georeferenced t-LiDAR data in PolyWorks and then imported into the SplitFx software for the calculation of both the fault plane and kinematic indicator orientations. SplitFx was used to create a triangulated mesh from the point cloud to identify the areas on the fault plane for orientation analysis. The limiting factors in SplitFx were the number and the size of the identified areas

(blue triangle in Fig. 3e) and their orientation to each other on the mesh. For these limiting factors some criteria were defined such as the number of points with a maximum edge length of 0.10 m, and a minimum of four neighbouring patches with a maximum 3° divergent angle to their respective neighbour. Subsequently, the dip direction and the dip of the fault plane are automatically defined on the 3-D meshed surface (Fig. 3e). The dip direction and dip of the slickenside lineation or striation can be calculated by using the PolyWorks software with the georeferenced data set. We used a simple method to calculate the 3D slip vector on the fault plane manually as a line between two points (Gold et al., 2012); the azimuth and the angle of the line are extracted (Fig. 4a).

After calculating the orientation of the fault plane, the direction of motion and the slickenside orientation, the palaeostress analysis can be performed. Slip vector analysis was undertaken using TectonicsFP version 1.7.5 software (Ortner et al., 2002). The obtained orientation and sense of movement data were inserted into the TectonicsFP software and the PBT method was used for the kinematic analysis, which comprises the theoretical construction of the strain axes with P as compressional, B as neutral and T as extensional axes.

The first step involved the input of the dip direction and dip of both the plane and lineation into the software followed by the sense information; the data are then corrected using a defined below 10° threshold error. The second step included the calculation

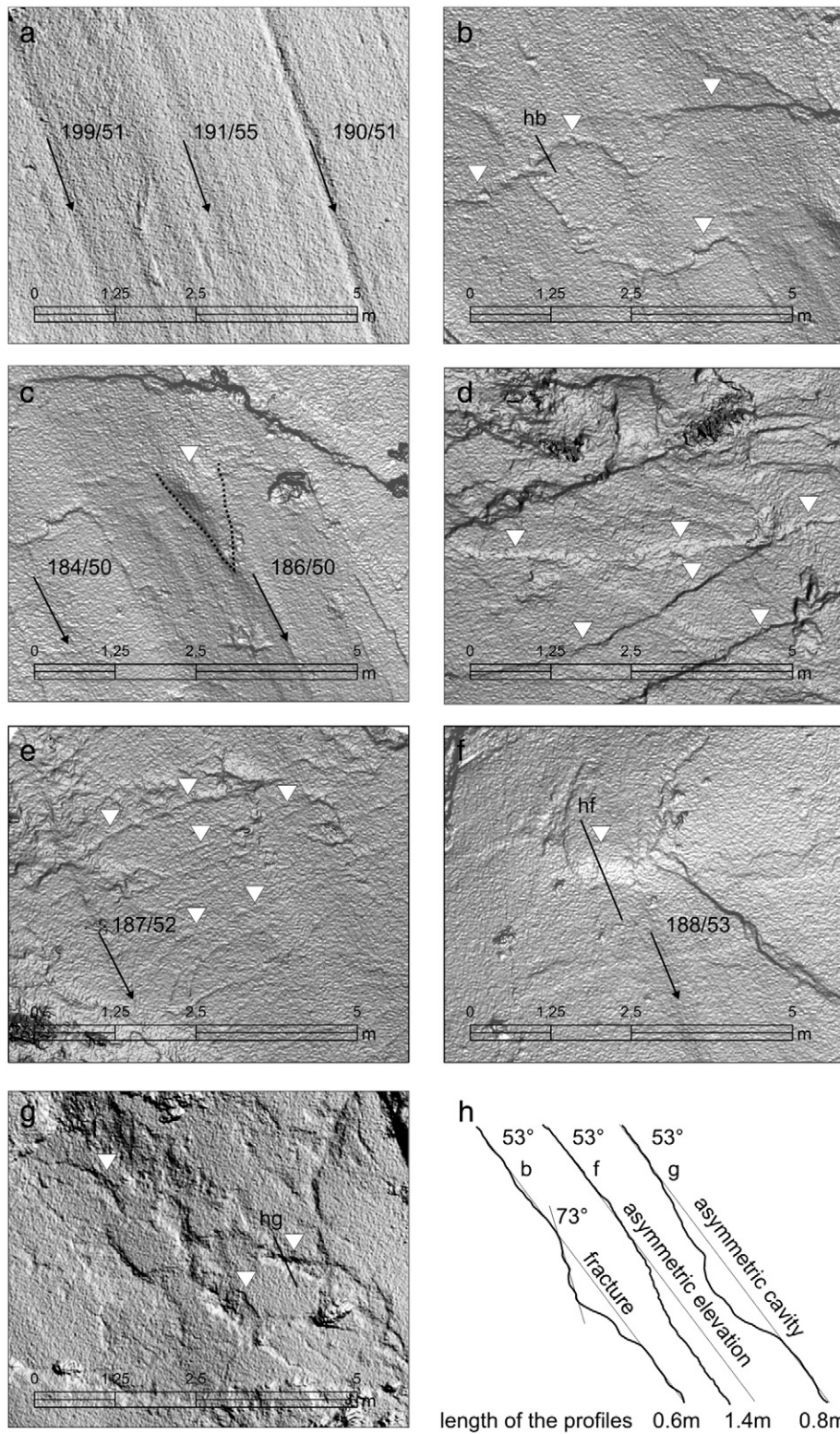


**Fig. 4.** Detailed view of location 1 using t-LiDAR data. The analysis of kinematics indicators on the bedrock fault plane shows that the Spili Fault has undergone normal faulting. The black arrows show the direction of movement and the white triangles refer to eight different kinematics indicators for normal faults: (a) the slickenside lineation; (b) synthetic hybrid fractures (hb section in h); (c) crescentic markings; (d) steps; (e) tension gashes perpendicular to the lineation orientation; (f) asymmetric elevation (hf section in h); (g) asymmetric cavity (hg section in h); (h) profiles taken from b, f and g.

of the theoretical pressure and tension axes of the orientation data, using an assumed friction angle of 30° (Reicherter and Peters, 2005; Sippel et al., 2009); several studies have shown better fitting results when applying a frictional angle of 30° for palaeostress data set instead of 45° which is typically used in seismological analysis (Angelier, 1994).

The third step was to obtain the palaeostress tensors and the axial ratio of the stress ellipsoid defined as  $\sigma_1 \geq \sigma_2 \geq \sigma_3$ , for the calculation of  $R = [(\sigma_2 - \sigma_3) / (\sigma_1 - \sigma_3)]$ . The ratio R has a value between 0 and 1, and indicates the stress regime for the individual scarp. These steps were then repeated using the manually obtained orientation data to

allow for the comparison with the t-LiDAR data and subsequent elevation. An error analysis between the two data sets was carried out in each case and included the mean calculated vector angle of the complete data sets. Furthermore, the divergent angle between the results of individual analyses includes the calculated value as a percentage. Lastly, all results of the t-LiDAR calculations were validated and compared to the compass extracted field results.

#### 4. Results

For each individual study location, the outcomes are: the orientation of the fault plane (dip direction and dip), the lineation (dip direction and dip of kinematic indicators) and the sense of the slip motion from the kinematic indicators. Manually collected field data comprises 34 measurements of fault plane orientation with the corresponding slickenside kinematics and sense of the motion from locations 1, 2 and 3. In contrast, the remote sensing data comprises 24 measurements from locations 1, 2, 3 and 4, which equates to 6 analysed results per t-LiDAR scanned location (see Table 1).

The mean dip direction and dip of the fault planes calculated from t-LiDAR measurements varies from west to east: 226/60 (location 1), 190/54 (location 2), 171/56 (location 3), and 170/42 (location 4); when all 24 measurements are combined the resulting mean dip direction and dip is 189/53. The mean dip direction and dip from manual field measurements also vary: 223/55 (15 values; location 1), 186/58 (10 values; location 2), and 171/62 (9 values; location 3); when all 34 measurements are combined the resulting mean dip direction and dip is 198/58. The differences between the calculated and measured fault plane mean orientation in degrees are 003/05 for location 1, 004/04 for location 2, and 000/06 for location 3; and the mean difference for all data is 009/05. The percentage divergence of the

manual field and remote sensing results are, therefore, around 0.8%, 1.1% and 0% for the dip direction and 5.5%, 4.4% and 6.6% for the dip at locations 1, 2 and 3 respectively. The summarised percentage difference of the complete data set between the t-LiDAR and field measurements amounts to 2.5/5.5% (009/05).

On every analysed fault plane we found slickensides, lineations and corrugations at different scales and in different conditions (Figs. 3, 4a). The mean dip direction and dip of these kinematic indicators from the t-LiDAR results are 198/50 (location 1), 181/53 (location 2), 225/49 (location 3), 209/33 (location 4), and 203/47 (all data). The manual field measurements are 212/50 (location 1), 201/57 (location 2), 218/49 (location 3) and 208/53 (all data). The degree differences between these two methods are 014/00 at location 1, 020/04 at location 2, 007/00 at location 3, and 005/06 using all data. The percentage divergence of lineation is 3.8, 5.5 and 1.9% for the dip direction and 0, 4.4 and 0% for the dip at locations 1, 2 and 3 respectively. The comparison of all data between t-LiDAR and manual field measurements is 1.4/6.6% (005/06), and in this case the mean t-LiDAR data are below the field data values. The mean error of the corrected data using TectonicsFP is between 1.3° and 2.7° for the manual field data, and between 1.8° and 3.8° for the t-LiDAR data.

The kinematic indicators show predominantly normal faulting. We found six definitive kinematic criteria on the fault plane to determine the sense of motion (see Fig. 4). Here, we present one significant example from location 1 where many kinematic indicators can be observed (see Figs. 1, 3, 4). The main kinematic indicators are the group of fractures, which are normally orientated perpendicular or sub-perpendicular to the slickenside lineation (Fig. 4b, e); these can be categorised as tension gashes or synthetic hybrid fractures. Typically, these fractures range in scale from a few centimetres to metres and form clusters on the polished fault plane. The penetration inclination

**Table 1**  
Station = study location along the Spili Fault from west to east (see Fig. 1) and the comparisons of the data sets;  $N$  = number of investigation measurements at individual location;  $\sigma_1$  = main compression direction,  $\sigma_2$  = intermediate direction,  $\sigma_3$  = main extension direction,  $R$  = axial ratio of the stress ellipsoid  $R = [(\sigma_2 - \sigma_3) / (\sigma_1 - \sigma_3)]$  with  $\sigma_1 > \sigma_2 > \sigma_3$ ; mean error of corrected data in TectonicsFP.

Station	Coordinates UTM 34	$N$	Mean dip direction/ dip (plane)	Mean dip direction/ dip (lineation)	$\sigma_1$	$\sigma_2$	$\sigma_3$	$R$	Mean error of corrected data in degrees (°)	Scan windows	Resolution in mm	Point numbers
<i>Field</i>												
1	276299/3898671/ 475	15	223/55	212/50	161/79	307/09	038/06	0.51	1.9			
2	278376/3897589/ 752	10	186/58	201/57	259/83	100/07	010/02	0.49	1.3			
3	284074/3893102/ 595	9	171/62	218/49	273/65	095/25	005/01	0.5	2.7			
All data		34	198/58	208/53	237/81	111/05	021/04	0.48	1.9			
<i>LiDAR</i>												
1	276299/3898671/ 475	6	226/60	198/50	143/74	297/14	028/07	0.49	3.8	2	5	5953500
2	278376/3897589/ 752	6	190/54	181/53	152/82	277/05	007/06	0.49	2.3	1	2	2667600
3	283976/3892934/ 554	6	171/56	225/49	276/64	101/26	010/02	0.49	1.8	1	20	2500000
4	284883/3892682/ 493	6	170/42	209/33	235/59	103/23	004/19	0.48	3.6	2	28	3306600
All data		24	189/53	203/47	227/77	104/04	013/09	0.53	2.9	6		14427700
<i>Difference in °</i>												
1			003/05	014/00	018/05	010/05	010/01	0.02				
2			004/04	020/04	107/01	177/02	003/04	0.00				
3			000/06	007/00	003/01	010/21	005/01	0.01				
All data			009/05	005/06	010/04	007/01	008/05	0.05				
<i>Divergence in %</i>												
1			0.8/5.5	3.8/0.0	5.0/5.5	2.7/5.5	2.7/1.1					
2			1.1/4.4	5.5/4.4	29/1.1	49/2.2	0.8/4.4					
3			0.0/6.6	1.9/0.0	0.8/1.1	2.7/23	1.4/1.1					
All data			2.5/5.5	1.4/6.6	2.7/4.4	2.1/1.1	2.2/5.5					
Complete data set		58	194/56	206/50	232/80	108/06	018/05	0.5	1.8			

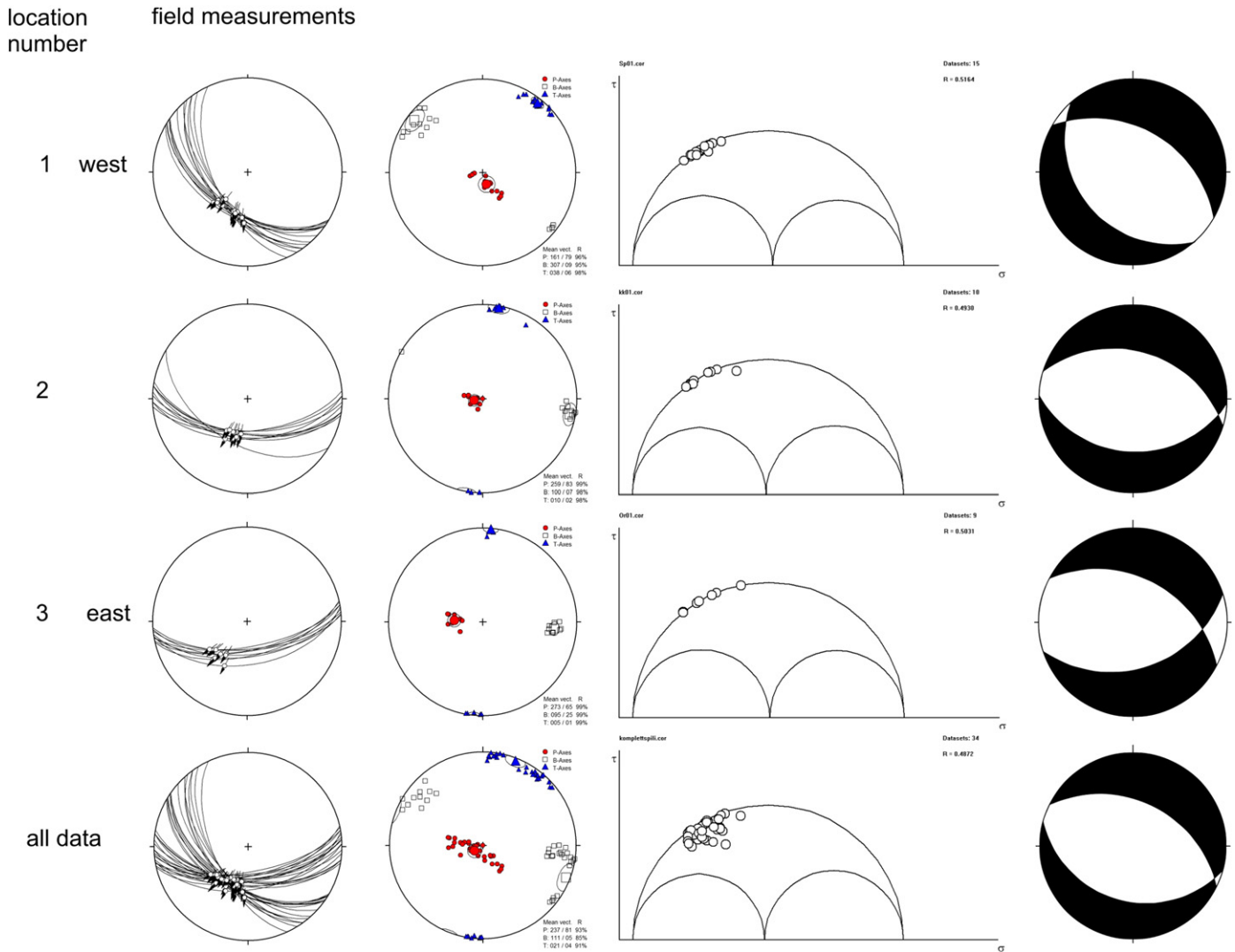


Fig. 5. Summary of reconstructed palaeostress from field data collected manually. The figure comprises the plot types at individual study locations as well as combined all data plots: Angelier plot, pt-axes plot (red circle: sigma 1, white square: sigma 2; blue triangle: sigma 3), Mohr's circle plot and fault plane solution (stereoplot).

angle down-slope into the fault surface is around 73° (Fig. 4hb). Generally, the penetration angle of these fractures is 75° or more (Doblas et al., 1997; Hancock and Barka, 1987). Another common group is the asymmetric cavities. This group includes asymmetric cavities with congruous steps (sometimes formed by Riedel shears), pluck holes and spall marks (Fig. 4g). Typically, they pull out the material on the footwall and leave a sharp edge on the upper part of their habitus (Fig. 4hg). Steps can also be observed on the fault plane, especially tension-related features. These features constitute three different types: sharp borders, tension fractures and detached fragments (Fig. 4d). Metre scale crescentic markings are poorly represented on the fault; however, these are good indicators for active normal faulting and are characterised by a carrot-shaped wedge (Fig. 4c). Also, when viewed at metre scale, the asymmetric elevation perpendicular to the movement direction shows down-slope steps (20 cm) on the fault plane (Fig. 4f, hf).

The results of the reconstructed palaeostress regime for both manual field and t-LiDAR measurements show a difference in degrees as follows: sigma 1 010/04, sigma 2 007/01 and sigma 3 008/05 at locations 1, 2 and 3 respectively. The percentage divergence of all data from manual field and t-LiDAR palaeostress investigations amounts to sigma 1 2.7/4.4%, sigma 2 2.1/1.1%, and sigma 3 2.2/5.5% (Table 1) for locations 1, 2 and 3 respectively. The axial ratio of the stress ellipsoid (R) calculated using all data

is around 0.5. The results of all comparison data (58 data sets) are summarised in Table 1.

### 5. Discussion and conclusions

The application of terrestrial remote sensing to determine the orientation of the fault plane and kinematic indicators for subsequent slip vector reconstruction in active tectonic environment was successfully carried out and the results were validated by comparison with manual field measurements. The method is an excellent tool for remote and non-contact present stress field investigations on inaccessible active bedrock faults and also allows fault scarps to be preserved and monitored for future investigations. The results of our investigations on the Spili Fault are similar to the findings of Monaco and Tortorici (2004) with a mean north-east and south-west extension direction (see Figs. 5, 6). Furthermore, using this method an abundance of information about fault conditions and geometry can be observed in a spatial three-dimensional way. The advantage of the t-LiDAR solution is the fast collection of high spatial resolution data, and in combination with conventional methods a quantitative improvement of results is ensured. For the reconstruction of the fault plane orientation, the summarised t-LiDAR data shows a small deviation to the field data; lower than 2.5% for the dip direction

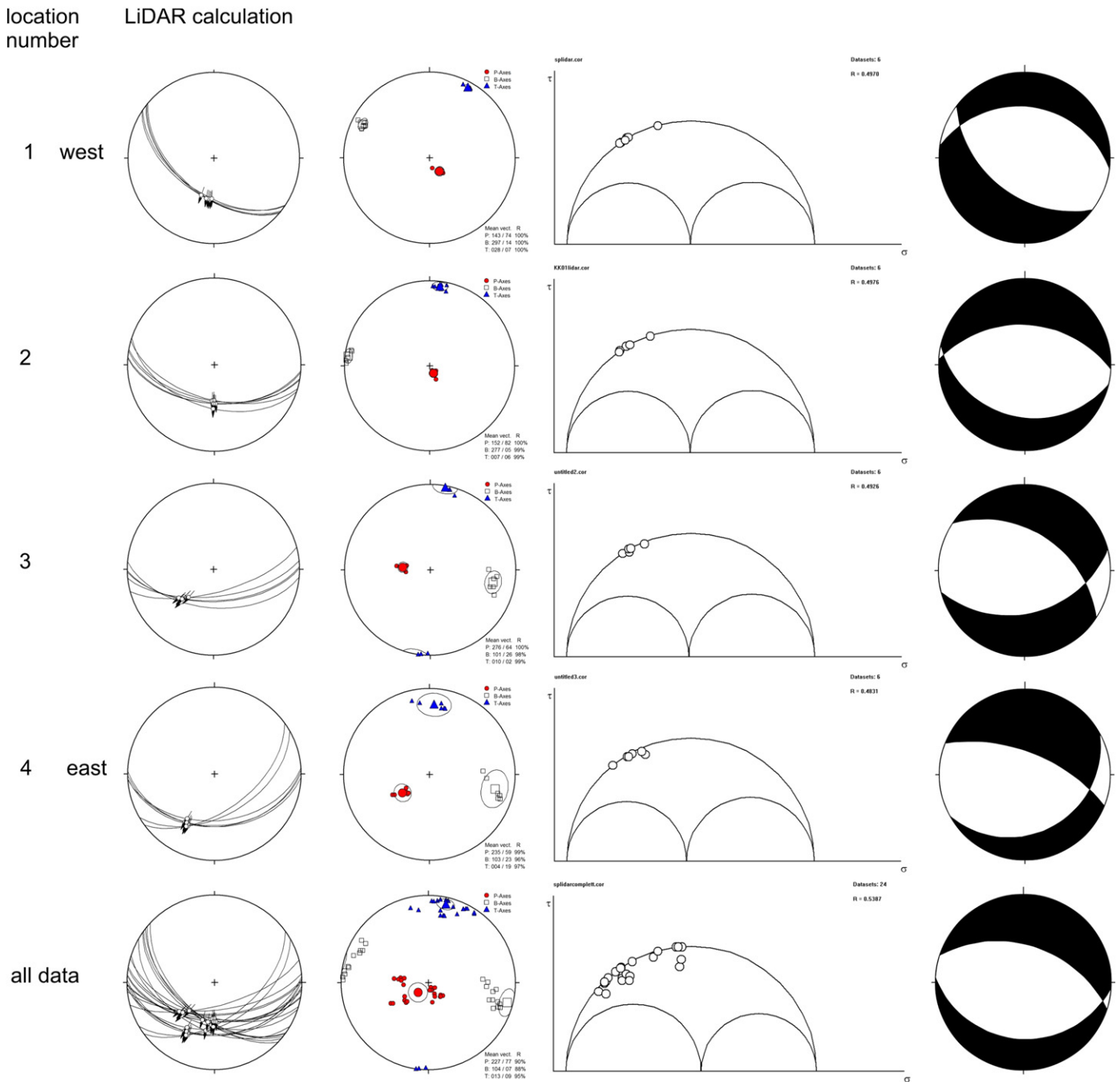


**Fig. 6.** Summary of reconstructed palaeostress from t-LiDAR data. The figure comprises the plot types at individual study locations as well as combined all data plots: Angelier plot, pt-axes plot (red circle: sigma 1, white square: sigma 2; blue triangle: sigma 3), Mohr's circle plot and fault plane solution (stereoplot).

and less than 5.5% for the dip. Hence, the threshold errors are  $\pm 4.5^\circ$  and  $\pm 2.5^\circ$  for dip direction and dip using the related vector angles (ca.  $\pm 005/03$ ). The three-dimensional analysis of the kinematic indicator orientation shows a mean percentage divergence of 1.4% for the dip direction and 6.6% for the dip. This implies a threshold for the corresponding angle of  $\pm 2.5^\circ$  and  $\pm 3^\circ$  (ca.  $\pm 003/03$ ) for the dip direction and dip.

By critically reviewing the data, the relatively large inaccuracy angle of the slickenside orientation (ca. 5.5%) and palaeostress tensors (ca. 49% for sigma 2) at location 2 is conspicuous. It turned out that, this is due to imprecise data recording of t-LiDAR view direction during the field data collection or point picking for the lineation orientation. The visual summary of all palaeostress data is shown in Figs. 5 and 6. The figures comprise different plot types at the study locations as well as combined

all data plots. The plot types include: the Angelier plot, the pt-axes plot (red circle: sigma 1, white square: sigma 2, blue triangle: sigma 3), the Mohr's circle plot, and the fault plane solution. The data obtained by t-LiDAR and conventional compass clinometer data are remarkably similar.

When all reconstructed stress data are taken into account, the percentage divergence is relatively small. The maximum mean percentage divergence of all sigma data has values of dip direction lower than 3% and dip lower than 6% (ca.  $\pm 005/03$ ). Combined, this means that there is an error of less than  $10^\circ$  between the t-LiDAR and manual field techniques.

Possible sources of error could be the manual collection of the pitch and roll angle of the TLS view direction. This error increases further with

distance. To negate this, an automatic registration in the t-LiDAR system would be helpful.

In this case study we have not used the panchromatic information. This photo image data could be used to characterise fault plane phenomena such as breccias, joints or to determine vegetated areas on the surface and requires further studies.

Further steps in our research will be studying reactivated fault planes with multiple kinematic indicators or striations in palaeofault systems in similar lithologies with t-LiDAR for stress reconstructions.

## Acknowledgement

This study was financially supported by the German Research Foundation (DFG project RE 1361/12-1) and by the RWTH Aachen University. We would like to thank Christoph Grützner for his fruitful and constructive criticism. Furthermore, we would like to thank the two reviewers (anonymous and Damien Delvaux) for the detailed remarks.

## Reference

- Angelier, J., 1994. Fault slip analysis and palaeostress reconstruction. In: Hancock, P.L. (Ed.), *Continental Deformation*. Pergamon Press, Oxford, pp. 53–101.
- Bonneau, M., 1984. Correlation of the Hellenides nappes in the south-eastern Aegean and their tectonic reconstruction. Special Publication of the Geological Society of London 17, 517–527.
- Brenner, C., 2005. Building reconstruction from images and laser scanning. *International Journal of Applied Earth Observation and Geoinformation* 6, 187–198.
- Candela, T., Renard, F., Bouchon, M., Brouste, A., Marsan, D., Schmittbuhl, J., Voisin, C., 2009. Characterization of fault roughness at various scales: implications of three-dimensional high resolution topography measurements. *Pure and Applied Geophysics*. <http://dx.doi.org/10.1007/s00024-009-0521-2>.
- Caputo, R., Catalano, S., Monaco, C., Romagnoli, G., Tortorici, G., Tortorici, L., 2010. Active faulting on the island of Crete (Greece). *Geophysical Journal International* 183, 111–126. <http://dx.doi.org/10.1111/j.1365-246X.2010.04749.x>.
- Doblas, M., 1998. Slickenside kinematic indicators. *Tectonophysics* 295, 187–197. [http://dx.doi.org/10.1016/S0040-1951\(98\)00120-6](http://dx.doi.org/10.1016/S0040-1951(98)00120-6).
- Doblas, M., Mahecha, V., Hoyos, M., López-Ruiz, J., 1997. Slickenside and fault surface kinematic indicators on active normal faults of the Alpine Betic Cordilleras, Granada, southern Spain. *Journal of Structural Geology* 19 (2), 159–170. [http://dx.doi.org/10.1016/S0191-8141\(96\)00086-7](http://dx.doi.org/10.1016/S0191-8141(96)00086-7).
- Fassoulas, C., 1999. The structural evolution of central Crete: insight into the tectonic evolution of the South Aegean (Greece). *Journal of Geodynamics* 27, 23–43. [http://dx.doi.org/10.1016/S0264-3707\(97\)00026-4](http://dx.doi.org/10.1016/S0264-3707(97)00026-4).
- Fassoulas, C., Kilias, A., Mountrakis, D., 1994. Postnappe stacking extension and exhumation of high-pressure/low-temperature rocks in the island of Crete, Greece. *Tectonics* 13, 127–138. <http://dx.doi.org/10.1029/93TC01955>.
- Gold, P.O., Cowgill, E., Kreylos, O., Gold, R.D., 2012. A terrestrial lidar-based workflow for determining three-dimensional slip vectors and associated uncertainties. *Geosphere* 8 (2), 431–442.
- Hancock, P.L., Barka, A.A., 1987. Kinematic indicators on active normal faults in western Turkey. *Journal of Structural Geology* 9 (5/6), 573–584. [http://dx.doi.org/10.1016/0191-8141\(87\)90142-8](http://dx.doi.org/10.1016/0191-8141(87)90142-8).
- Hu, H., Fernandez-Steeger, T.M., Azzam, R., 2012. Numerical modeling of LiDAR-based geological model for landslide analysis. *Automation in Construction* 24, 184–193.
- InnovMetric: Polyworks, 2010. 3-D scanner and 3-D digitizer software from InnovMetric Software Inc. available at: <http://www.innovmetric.com/Manufacturing/home.aspx>.
- Jones, R.R., Kokkalas, S., McCaffrey, K.J.W., 2009. Quantitative analysis and visualization of nonplanar fault surfaces using terrestrial laser scanning (LiDAR)—the Arkitsa fault, central Greece, as a case study. *Geosphere* 5 (6), 465–482. <http://dx.doi.org/10.1130/GES00216.1>.
- Kokkalas, S., Jones, R.R., McCaffrey, K.J.W., Clegg, P., 2007. Quantitative fault analysis at Arkitsa, central Greece, using terrestrial laser-scanning (“LiDAR”). *Bulletin of Geological Society of Greece*, vol. XXXVII.
- Krijgsman, W., 1996. Miocene magnetostratigraphy and cyclostratigraphy in the Mediterranean: extension of the astronomical polarity time scale. Unpublished PhD thesis, University of Utrecht.
- Ma, X.Q., Kusznir, N.J., 1995. Coseismic and postseismic subsurface displacements and strains for a dip-slip normal fault in a three-layer elastic-gravitational medium. *Journal of Geophysical Research* 100, 12813–12828.
- Maniatis, G., Hampel, A., 2008. Along-strike variations of the slip direction on normal faults: insights from three-dimensional finite-element models. *Journal of Structural Geology* 30, 21–28.
- Meulenkamp, J.E., Wortel, M.J.R., Van Wamel, W.A., Spakman, W., Hoogerduyn Strating, E., 1988. On the Hellenic subduction zone and the geodynamical evolution of Crete since the late Middle Miocene. *Tectonophysics* 146, 203–215. [http://dx.doi.org/10.1016/0040-1951\(88\)90091-1](http://dx.doi.org/10.1016/0040-1951(88)90091-1).
- Meulenkamp, J.E., van der Zwaan, G.J., van Wamel, W.A., 1994. On late Miocene to recent vertical motions in the Cretan segment of the Hellenic arc. *Tectonophysics* 234, 53–72.
- Michetti, A.M., Ferrel, L., Esposito, E., Porfido, S., Blumetti, A.-M., Vittori, E., Serva, L., Roberts, G.P., 2000. Ground effects during the 9 September, 1998, Mw=5.6, Lauria earthquake and the seismic potential of the “Aseismic” Pollino region in Southern Italy. *Seismological Research Letters* 71, 31–46.
- Monaco, C., Tortorici, L., 2004. Faulting and effects of earthquakes on Minoan archaeological sites in Crete (Greece). *Tectonophysics* 382, 103–116. <http://dx.doi.org/10.1016/j.tecto.2003.12.006>.
- Mouslopoulou, V., Moraetis, D., Fassoulas, C., 2011. Identifying past earthquakes on carbonate faults: advances and limitations of the ‘Rare Earth Elements’ method based on analysis of the Spili Fault, Crete, Greece. *Earth and Planetary Science Letters* 309, 45–55. <http://dx.doi.org/10.1016/j.epsl.2011.06.015>.
- Nguyen, H.T., Fernandez-Steeger, T.M., Wiatr, T., Rodrigues, D., Azzam, R., 2011. Use of terrestrial laser scanning for engineering geological applications on volcanic rock slopes — an example from Madeira island (Portugal). *Natural Hazards and Earth System Sciences* 11 (1–11), 2011. <http://dx.doi.org/10.5194/nhess-11-1-2011>.
- Ortner, H., Reiter, F., Acs, P., 2002. Easy handling of tectonic data: the programs TectonicVB for Mac and Tectonics FP for Windows(tm). *Computers & Geosciences* 28, 1193–1200.
- Papanikolaou, I.D., Roberts, G.P., 2007. Geometry, kinematics and deformation rates along the active normal fault system in the Southern Apennines: implications for fault growth. *Journal of Structural Geology* 29, 166–188.
- Papanikolaou, D., Vassilakis, E., 2010. Thrust faults and extensional detachment faults in Cretan tectonostratigraphy: implications for Middle Miocene extension. *Tectonophysics* 488, 233–247.
- Peterek, A., Schwarze, J., 2004. Architecture and Late Pliocene to recent evolution of outer-arc basins of Hellenic subduction zone (south-central Crete, Greece). *Journal of Geodynamics* 38, 19–55.
- Reicherter, K.R., Peters, G., 2005. Neotectonic evolution of the central Betic Cordilleras (southern Spain). *Tectonophysics* 405 (1–4), 191–212. <http://dx.doi.org/10.1016/j.tecto.2005.05.022>.
- Roberts, G.P., 1996. Variation in fault-slip directions along active and segmented normal fault systems. *Journal of Structural Geology* 18 (6), 835–845. [http://dx.doi.org/10.1016/S0191-8141\(96\)80016-2](http://dx.doi.org/10.1016/S0191-8141(96)80016-2).
- Roberts, G.P., Michetti, A.M., 2004. Spatial and temporal variations in growth rates along active normal fault systems: an example from Lazio-Abruzzo, central Italy. *Journal of Structural Geology* 26, 339–376.
- Sagy, A., Brodsky, E.E., Axen, G.J., 2007. Evolution of fault-surface roughness with slip. *Geology* 35, 283–286. <http://dx.doi.org/10.1130/G23235A.1>.
- Scheffers, A., Scheffers, S., 2007. Tsunami deposits on the coastline of west Crete (Greece). *Earth and Planetary Science Letters* 259, 613–624. <http://dx.doi.org/10.1016/j.epsl.2007.05.041>.
- Schumann, A., Arndt, D., Wiatr, T., Götz, A.E., Hoppe, A., 2011. High-resolution terrestrial laser scanning and 3D modeling of a mineral deposit for extraction management optimization. *Zeitschrift der Deutschen Gesellschaft für Geowissenschaften* 162 (4), 435–442.
- Sippel, J., Scheck-Wenderoth, M., Reicherter, K., Mazur, S., 2009. Paleostress states at the south-western margin of the Central European Basin System — application of fault-slip analysis to unravel a polyphase deformation pattern. *Tectonophysics* 470, 129–146. <http://dx.doi.org/10.1016/j.tecto.2008.04.010>.
- Stewart, I.S., Hancock, P.L., 1990. Brecciation and fracturing within neotectonic normal fault zones in the Aegean region. In: Knipe, R.J., Rutter, E.H. (Eds.), *Deformation Mechanisms, Rheology and Tectonics*. Geological Society — Special Publications, 54, pp. 105–112.
- Stewart, I.S., Hancock, P.L., 1991. Scales of structural heterogeneity within neotectonic normal fault zones in the Aegean region. *Journal of Structural Geology* 13 (2), 191–204. [http://dx.doi.org/10.1016/0191-8141\(91\)90066-R](http://dx.doi.org/10.1016/0191-8141(91)90066-R).
- Stiros, S., 2001. The AD 365 Crete earthquake and possible seismic clustering during the fourth to sixth centuries AD in the Eastern Mediterranean: a review of historical and archaeological data. *Journal of Structural Geology* 23, 545–562. [http://dx.doi.org/10.1016/S0191-8141\(00\)00118-8](http://dx.doi.org/10.1016/S0191-8141(00)00118-8).
- Zachariasse, W.J., van Hinsbergen, D.J.J., Fortuin, A.R., 2011. Formation and fragmentation of a late Miocene supradetachment basin in central Crete: implications for exhumation mechanisms of high-pressure rocks in the Aegean forearc. *Basin Research*. <http://dx.doi.org/10.1111/j.1365-2117.2011.00507.x>.